From Images to Hydrologic Networks - Understanding the Arctic Landscape with Graphs

Tabea Rettelbach
tabea.rettelbach@awi.de
Alfred Wegener Institute Helmholtz Centre for Polar and Marine Research
Potsdam, Germany

Moritz Langer
moritz.langer@awi.de
Alfred Wegener Institute Helmholtz Centre for Polar and Marine Research
Potsdam, Germany

Ingmar Nitze
ingmar.nitze@awi.de
Alfred Wegener Institute Helmholtz Centre for Polar and Marine Research
Potsdam, Germany

Benjamin M. Jones
bmjones3@alaska.edu
University of Alaska Fairbanks
Fairbanks, Alaska, USA

Veit Helm
veit.helm@awi.de
Alfred Wegener Institute Helmholtz Centre for Polar and Marine Research
Bremerhaven, Germany

Johann-Christoph Freytag
freytag@informatik.hu-berlin.de
Humboldt-Universität zu Berlin
Berlin, Germany

Guido Grosse
guido.grosse@awi.de
Alfred Wegener Institute Helmholtz Centre for Polar and Marine Research
Potsdam, Germany

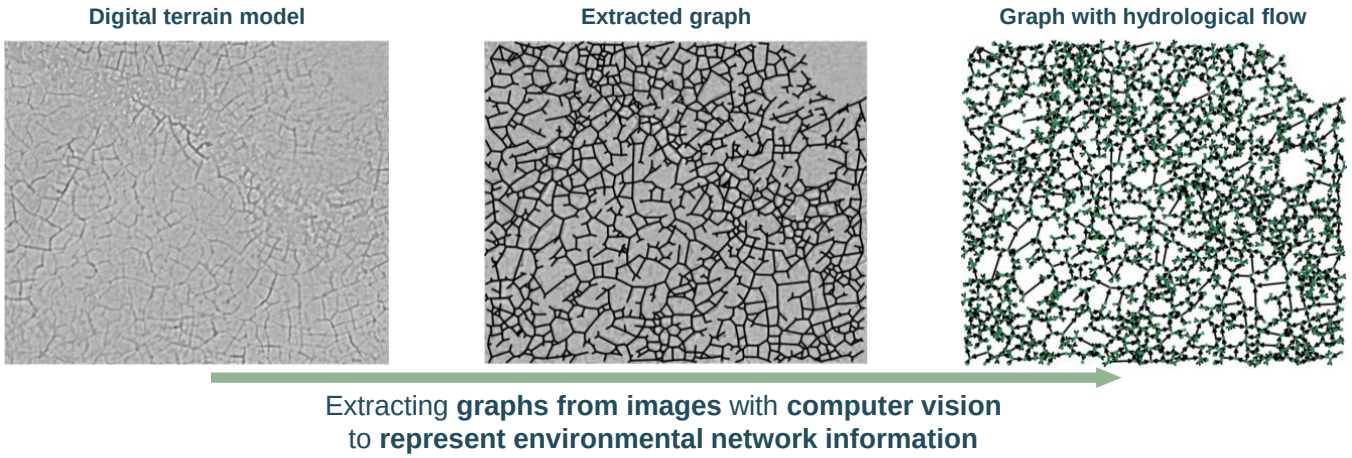

Figure 1: Using computer vision and graph analysis to detect networks in (Earth observation) imagery and analyze their environmental parameters with graph metrics.

ABSTRACT

Remote sensing-based Earth Observation plays an important role in assessing environmental changes throughout our planet. As an image-heavy domain, the evaluation of the data strongly focuses on statistical and pixel-based spatial analysis methods. However, considering the complexity of our Earth system, there are some environmental structures and dependencies that are not possible to accurately describe with these traditional image analysis approaches. One example for such a limitation is the representation of (spatial) networks and their characteristics. In this study, we thus propose a computer vision approach that enables the representation of semantic information gained from images as graphs. As an example, we investigate digital terrain models of Arctic permafrost landscapes with its very characteristic polygonal patterned ground. These regular patterns, which are clearly visible in high-resolution image and elevation data, are formed by subsurface ice bodies that are very vulnerable to rising temperatures in a warming Arctic. Observing these networks' topologies and metrics in space and time with graph analysis thus allows insights into the landscape's complex geomorphology, hydrology, and ecology and therefore

SSDBM 2022, July 6–8, 2022, Copenhagen, Denmark

ACM ISBN 978-1-4503-9667-7/22/07.
https://doi.org/10.1145/3538712.3538740

helps to quantify how they interact with climate change. We show that results extracted with this analytical and highly automated approach are in line with those gathered from other manual studies or from manual validation. Thus, with this approach, we introduce a method that, for the first time, enables upscaling of such terrain and network analysis to potentially pan-Arctic scales where collecting in-situ field data is strongly limited.

CCS CONCEPTS

• **Computing methodologies** → **Image representations**; **Image segmentation**; • **Mathematics of computing** → **Graphs and surfaces**; **Paths and connectivity problems**; • **Human-centered computing** → **Graph drawings**; **Geographic visualization**.

KEYWORDS

graph analysis, computer vision, digital terrain models, spatial data

ACM Reference Format:
Tabea Rettelbach, Moritz Langer, Ingmar Nitze, Benjamin M. Jones, Veit Helm, Johann-Christoph Freytag, and Guido Grosse. 2022. From Images to Hydrologic Networks - Understanding the Arctic Landscape with Graphs. In *34th International Conference on Scientific and Statistical Database Management (SSDBM 2022), July 6–8, 2022, Copenhagen, Denmark.* ACM, New York, NY, USA, 10 pages. https://doi.org/10.1145/3538712.3538740

1 INTRODUCTION

In the field of remote sensing-based Earth observation (EO), imaging sensors aboard satellites, aircraft, or uncrewed aerial vehicles (UAV) image or scan the Earth's surface, collect reflective information and store the sensed quantities as images. Researchers evaluate this data (typically stored as three-dimensional arrays) with computer vision and remote sensing image analysis techniques to identify spatial patterns of quantified variables and their interdependencies. Especially in environmental sciences, this approach enables an incredibly vast range of research, reaching across ecological, geological, meteorological, and oceanographic applications, to name a few. However, to answer some of the pertinent scientific questions, spatial and statistical pixel analysis can in times lack complexity to describe the underlying (environmental) structures of interest. In such cases, it is then necessary to rethink the way we represent the available information.

A prominent example, where pixel-based analyses reveal their inherent limitations, is encountered when we aim to describe networks and their characteristics. It is not possible to access raw pixel information from imagery and make assumptions about a landscape's connectivity, the topology, or the spatial relationship. In order to analyze network-like structures, we thus need to translate the information into other data structures, such as graphs. The challenge is then to find an appropriate method to translate the image-based information into a graph's edges and vertices.

In other image-heavy scientific disciplines, such as microbiology or medicine, similar approaches have been initially explored in the past decade. For example, researchers have generated graphs from microscopic images of leaf venation patterns [10, 30], of slime molds [2], and even of fracturing solids [22]. In EO however, this methodology has seemingly only gained traction in very recent years. Here, scientists explored the potential of representing road networks [16], river pathways [9, 25, 39], or agricultural fields [38] from satellite imagery as graphs in order to e.g., generate accurate road maps, describe river topologies, or gather statistics on agricultural spaces, respectively. However, we see that by adapting these kind of approaches, we may also gain valuable insights into processes that have direct implications to our environment under a changing climate.

In this study, we introduce an imagery-to-graph approach to investigate characteristic surface features predominantly found in thawing permafrost landscapes of the Arctic: polygonal patterned ground. By describing such landscapes and their inherent hydrology as (labeled) graphs, we are able to investigate their characteristic network structures with graph analysis metrics. Our graph extraction methodology is largely automated, modular, and partially parallelized. We present a three-tiered analytical approach, which consists of (a) the segmentation of imagery and subsequent representation of relevant information as graphs, (b) the morphological terrain analysis based on localized elevation information, and (c) the characterization of the real-world network based on the evaluation of graph analysis metrics computed for the extracted graph.

In the next chapter, we introduce the polygonal permafrost structures of interest in detail and highlight the relevance of understanding the network properties of these vulnerable permafrost landscapes in the context of climate change. In Chapter 3, we introduce the algorithmic approach and elucidate the requirements for the graph properties when extracting their structure from the EO imagery. Then, we showcase the functionality of the methodology based on exemplary data from a study site in northern Alaska in Chapter 4. Finally, we conclude with a synthesis and highlight potential integration of the introduced methods for future research.

2 BACKGROUND AND MOTIVATION

In the Earth's global carbon cycle, permafrost soils act as one of the planet's major carbon sinks. Permafrost itself is defined as any ground that stays at or below 0° C for at last two consecutive years [7]. With approximately 800 to 1000 Petagrams of frozen organic carbon [17, 32], permafrost stores approximately the same amount of carbon as the Earth's atmosphere. Permafrost ground covers circa 15 % of the northern hemisphere's landmass [27], and the largest domains can be found throughout the Arctic in Scandinavia, Russia, Alaska, Canada, and Greenland [28]. Globally rising atmospheric temperatures however, initiate warming and thawing of these soils. Especially in organic-rich ground, permafrost thaw promotes microbial activity and thus triggers the decomposition of soil carbon [12]. This process in turn allows the release of greenhouse gases (CO_2 and CH_4) into the atmosphere, which again leads to further increasing atmospheric temperatures [26]. Such a carbon feedback loop can have severe consequence for the environmental well-being of our Earth. It is thus incredibly important to monitor these strongly affected landscapes as to gain detailed insights and prepare for appropriate mitigation strategies.

Permafrost thaw can happen both through abrupt and through gradual thaw processes and they display in a great variety of ways. For permafrost that contains large amounts of ground ice, common

observable consequences are e.g., the initiation and progression of retrogressive thaw slumps (landslides typical in permafrost regions), coastal erosion, thermokarst lake formation and drainage, and ground subsidence. In ice-rich ground, a very widespread feature are regularly patterned ice-wedge polygons [4]. Through thermal contraction of ground in the very cold Arctic winter, frost cracks form in polygonal patterns throughout the soil. These thin but deep open fissures fill with meltwater once snow melts in spring and nearly vertical ice veins, connected in a polygonal pattern, form and slightly expand the cracks. This way, over the course of centuries to millenia, the ice veins can grow to large wedge-shaped ice bodies along the polygonal frost-cracking pattern, which will alter the morphology of the terrain [15, 21, 24]. In the initial and stable state, we usually observe low-centered polygons (LCPs), as the ice wedges (which define the borders of the polygons) elevate the ground to relative higher elevations compared to the center of the polygons (see Fig. 2 a). Typically, the elevation difference lies between 0.1 and 1.3 m [19, 34, 40]. However, with ongoing thaw, these landscapes undergo extensive morphological transition due to the differential subsidence following melt of ice wedges in the ground [23]. We then observe landscapes with high-centered polygons (HCP), as seen in Fig. 2 c. With the current warming trends, these topographical changes can be observed over multiple decades in undisturbed terrain. In disturbed permafrost terrain on the other hand, for example in landscapes that have recently experienced an intense wildfire, the transition from LCP to HCP happens on considerably shorter timescales of only several years [20]. This can be ascribed to the burned and removed uppermost organic soil layer which, in undisturbed terrain, otherwise acts as insulation for the permafrost below. Liljedahl et al. [23] observed and modeled the implications this morphological change has on the surface hydrology within the overall very flat landscape. They described how in LCP terrain, water accumulates in the largely isolated polygon centers, while with ongoing degradation, the surface water shifts towards the newly formed troughs. Due to a higher thermal capacity, ponded water in such troughs however promotes further melting of the ice wedges below and thus the further degradation of the landscape. Only when ice-wedge degradation has progressed considerably, and the individual initial troughs have connected to form a coherent network, will this water be able to drain out of the landscape, thus slowing or possibly stabilizing the degradation process.

Liljedahl et al. [23] described the phenomenon on very detailed scales based on local field investigations in Alaska, Canada, and Russia and verified their findings with high-resolution satellite imagery from dates between the 1950s and 2009. As polygonal patterned ground is widely distributed in the Arctic, a scalable mapping approach is needed for investigations on pan-Arctic scales. In [20], the authors investigated the ground subsidence and increase in roughness of thawing ice-wedge terrain using laser scanning-based elevation data and very high resolution satellite data in a fire scar in northern Alaska between 2009 and 2014. While it is possible to upscale this approach to larger areas (given data availability), it does not provide very detailed insights into the hyper-local process, but broadly quantifies rates of subsidence and roughness changes for larger spatial entities only. Further studies have also investigated the morphology (and changes therein) of polygonal landscapes,

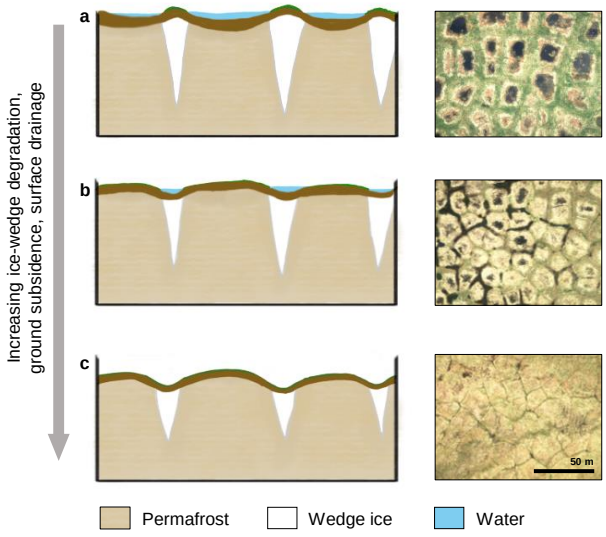

Figure 2: (a) Undegraded ice-wedge terrain is characterized by low-centered polygons (LCP), with water accumulating in the isolated polygon centers. (b) With ongoing thaw and increased ice melt, soil above ice wedges subsides to lower elevations, initiating landscapes with high-centered polygons. Water accumulates in the newly formed troughs along the polygon borders. (c) When thawing continues further, more troughs initiate between polygons and network connectivity increases, allowing water to drain from the landscape. The right column shows multi-spectral aerial images of the permafrost terrain in the respective stages of degradation. Imagery taken with the DLR Modular Airborne Camera System (MACS) on board AWI's Polar-6 plane in Northwest Alaska in July 2021.

however, again, none of them have enabled the quantification of very local details over large study areas [19, 34, 40].

While we are generally interested in the bigger picture of Arctic permafrost thaw, it is important to consider that also very local processes can have far-reaching impacts to extensive landscapes. In the scenario of ice-rich permafrost terrain, it is the initiation of single troughs above ice wedges that can considerably change the topology of polygonal networks and thus influence the hydrology, and subsequently the biogeochemistry, of entire catchments. It is therefore evident that methods to quantify the described changes, need to both be able to capture the very fine details, and simultaneously be scalable for investigating very large spatial domains (up to pan-Arctic scales).

We believe that the detection of the polygonal networks from EO data and their representation as graphs can achieve exactly this.

3 ALGORITHMIC FRAMEWORK

In order to adequately represent and analyze the polygonal thaw-affected landscapes as graphs, we introduce a highly modular, three-tiered approach. In the first module, we use traditional computer

vision algorithms on elevation information (digital terrain models, DTMs) represented as grayscale images to extract the topology of the polygonal networks and build them as graphs. For the second module, we investigate the topographical surroundings of each segmented trough and infer the morphological parameters of channel height and width using computer vision and function analysis. We then populate these results into the graphs as edge parameters. And lastly, we investigate (hydrological) characteristics of the network by leveraging traditional graph analysis metrics. Our approach is entirely implemented with Python and mainly relies on the joblib [36], networkx [13], numpy [14], opencv [5], scikit-image [35], scipy [37], and sknw [42] libraries.

3.1 From Images to Graphs

In order to represent the polygonal permafrost network as graphs, we represent each trough (channel at the edge of two polygons) as a graph edge and each intersection of troughs at the polygons' corners as vertices. Prior to building the graph of the ice-wedge network however, we need to establish the topological requirements that are necessary to accurately represent the underlying real-world properties:

- *Planarity.* Since we are looking at the Earth's surface, troughs are not allowed to cross paths without meeting at a trough intersection. This needs to be reflected within the graph.
- *Directionality.* As water flow generally follows the surface gradient, each edge E has a clear directionality. E is therefore represented by an ordered pair of vertices (s, t), for which s always lies at higher elevations than t. The directionality thus represents the direction of hydrological flow in the landscape.
- *Acyclicity.* Again, considering the downslope gradient of surface water flow, the graph must invariably be acyclical.

As we define the edges and vertices from data represented in two-dimensional space, the condition of planarity is fulfilled. Any seemingly crossing troughs are already on the same plane and would thus create a new intersection and therefore define the location of another vertex. Further, considering that the network in question is based on physical surface properties, and the directionality of E is inferred from the relative height h of s and t, the condition of acyclicity is inherently given. Any cycle in the graph would thus imply the existence of a Penrose staircase situation. For edges E with $h_s = h_t$, we nevertheless set a directionality and define it based on the condition of acyclicity remaining preserved.

In order to satisfy these conditions when extracting the graph, we make use of a methodology previously introduced by Xiaolong and Christensen [42] which converts image skeletons into vertices and edges. An image skeleton is a topological representation of morphological shapes in a binary image [33]. To identify the skeletons of the troughs, we must thus first binarize the underlying data, to have it represent the troughs as foreground class and any other landscape as background.

Multiple approaches to segmenting EO imagery or elevation data to identify polygonal troughs have been published in the last several years [1, 3, 41, 44]. Most of them rely on convolutional neural networks (standard CNN, Mask R-CNN, U-Net) and the introducing studies showed high prediction accuracies for locating the polygons (or the troughs in-between). While these approaches where highly reproducible for the investigated locations in the respective studies, the algorithms unfortunately did not transfer well to other study sites, including ours, and could not accurately segment the troughs from any other landscape feature. Thus, we introduce an analytical algorithmic approach to achieve the segmentation that relies on traditional computer vision and morphological image analysis:

(1) *Thresholding.* In HCP landscapes, we can assume that troughs always lie at relative lower elevations than the polygons. We therefore use an adaptive threshold to segment the troughs from the polygons. Instead of binarizing the DTM based on a global threshold T_g, the adaptive thresholding method convolves a kernel k_w with w being the user-defined width of the kernel, over the image and computes individual thresholds T_k for each investigated neighborhood N_k based on $T_k = mean(N_k) - C$. C is an optional scalar and used for finetuning. When calculating the mean of N_k, we further weight the pixels based on a Gaussian distribution from the kernel's center pixel. The output represents the likely trough pixels as foreground (1) and any other pixels as background (0).
(2) *Cleaning.* Especially in relatively flat areas of the landscape, the adaptive threshold introduces impulse noise. We eliminate this pepper noise (individual foreground pixels in-midst of a background cluster) by assuming that any isolated trough pixels or smallest clusters thereof are noise and assigning these pixels to the background class. To eliminate any salt noise (individual background pixels in-midst of a foreground cluster), and to connect troughs that might have just missed being connected by a few pixels, we use morphological closing. This means growing any clusters of foreground class by x pixels at the outer edges and subsequently eroding the structure by x pixels again. Connections that were initiated with the growing, do not separate again when eroding.
(3) *Skeletonization.* Once the noise is brought to a minimum, the troughs should be adequately represented by the foreground class of the binary image and can be skeletonized using Zhang's method [43]. For this step, we consider the 8-neighborhood. That is, we allow both straight and diagonal connections for the skeleton pixels.

Following this analytical approach, we achieve segmentation accuracies that are on a par with the above-mentioned machine learning approaches (cf. Chapter 4) [1, 3, 41, 44]. Furthermore, this approach eliminates the need of large (labeled) training sets and therefore requires far less expert knowledge for inference. However, given the modular setup of our introduced methodology, the usage of alternative trough segmentation algorithms is nevertheless still possible for the interested user. The only requirement to compute the skeleton (from which the graph needs to be drawn) is a binary representation of the data, where all trough pixels need to belong to the foreground class.

From the skeleton of the trough network, we can then infer the underlying graph as follows: Each foreground pixel and its eight immediate neighboring pixels are investigated. Any foreground pixel that neighbors exactly two other foreground pixels will be

considered as edge pixel. All other foreground pixels will be represented as vertices. Vertices that are connected by edge pixels will be connected by an actual edge in the graph. Generally, we aim to simplify the representation of the landscape, however, we must not forget that we still intend to represent it as accurate as possible. We therefore retain the information on the original path of the trough in pixel coordinates as edge weights.

All steps of the first module scale with $O(n \cdot m)$ with n and m being the height and width of the input terrain image in pixels.

3.2 From Terrain Properties to Graph Parameters

As we are not only interested in the topology of the network as a whole, but also in the morphology of the individual troughs, we must determine their width and depth from the terrain model as well. This information is particularly of interest for multi-temporal investigations of a landscape. A fast eroding trough, i.e., a trough for which its depth and width are increasing over time, is likely to connect with neighboring troughs in the near future. We thus determine averages for both parameters for each channel and store the information as weights in the corresponding edge.

To determine the depth and width of a trough, we look at cross-sectional elevation profiles (transects) at each pixel p along the channel's course of pixels. All transects are located approximately perpendicular to the course of the channel. The perpendicularity is determined based on the alignment of the immediate predecessor $p-1$ and the immediate successor $p+1$ of pixel p under investigation. Figure 3 visually conveys the five possible cases of pixel constellations (and their $\pi/2$-rotation-symmetrically equivalent settings) and how we extracted the respective transects.

Following this approach, we distinguish between straight and diagonal transects which, although each capturing the same number of pixels l_p have different real-world lengths l_t. l_t is therefore dependent on the orientation of the transect as well as the spatial resolution r of the underlying data and follows

$$l_t = \begin{cases} l_p \cdot r & \text{for cases } a, b, d, \text{ and } e \text{ of Fig. 3} \\ l_p \cdot r \cdot \sqrt{2} & \text{for case } c \text{ of Fig. 3.} \end{cases} \quad (1)$$

As these channels are real-world structures, each transect is unique in shape. However, it is possible to approximate and thus describe the profile with a Gaussian function

$$f(x; \mu, \sigma^2) = \frac{1}{\sqrt{2\pi\sigma^2}} e^{\frac{(x-\mu)^2}{2\sigma^2}}, \quad (2)$$

μ being the location and σ the scale of the distribution. The distribution's full width at half maximum (FWHM, FWHM $= 2\sqrt{2ln2} \cdot \sigma$) and $f(\mu)$ are then considered as proxies for the transect's width and depth respectively.

While fitting the Gaussian function to the extracted elevation profiles scales with $O(e)$, e corresponding to the number of edge pixels, it is nevertheless rather compute intensive. By providing bounds to possible values for σ (based on typical real-world widths of the troughs) we managed a computational speed-up of already more than 300 %. We further implemented data parallelism and distributed the curve-fitting processes to all available cores of the CPU. We used the joblib.Parallel library [36] with the loky backend

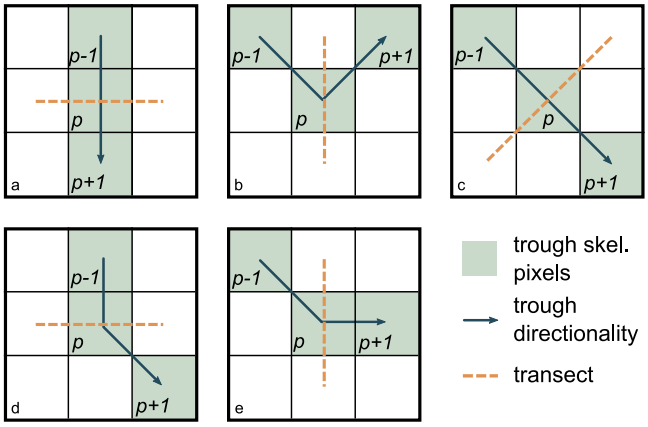

Figure 3: Cross-sections for investigating the trough morphologies must ideally be placed perpendicular to the course of the troughs with $s = [p-1, p, p+1]$. For each transect (blue arrow) at trough skeleton pixel p (green, center pixels in each example), we thus investigate the respective locations of the two neighboring skeleton pixels $p-1$ and $p+1$ (also green) in respect to p. We identify five possible pixel-constellation scenarios (plus their $\pi/2$-rotation-symmetrically equivalent settings). For each setting, the orientation of the transect is shown by a dashed red line. In a, b, and c, the transect is strictly perpendicular to the tangent of s in p, while d and e have transects perpendicular to paths $s = [p-1, p]$ and $s = [p, p+1]$, respectively [31]. Figure adapted from Rettelbach et al. [31], licensed under CC BY; Licensee MDPI, Basel, Switzerland.

to enable multi-processing over concurrent Python worker processes. Our code largely relies on Python objects and is therefore not thread-safe under the Python Global Interpreter Lock. Threading could therefore not accelerate computation, and we accepted the slightly larger communication overhead that is necessary with the loky backend.

3.3 From Graphs to Hydrology

In this third module, we make use of common graph analysis metrics to infer hydrological properties of the thawing permafrost landscape based on the previously extracted graph with its populated edge parameters. In particular, we are interested in the following metrics:

- *Number of edges.* This corresponds to the number of troughs in the landscape. It allows a first estimate of the size of the hydrological network. As we also retained information on the original course of the trough's pixels, we can further retrieve the total length of all established channels and thus quantify the amount of all possible waterways.
- *Node degree.* This metric gives an estimate of the complexity of hydrologic connectivity within the network. Landscapes represented by graphs with a higher number of vertices (nodes) with degree 1 (i.e., dead ends), are likely in transition. The edges connected to these vertices represent troughs that

have likely only recently initiated and thus have not yet fully connected to other troughs in the vicinity.

- *Number of sources and sinks.* A source vertex in a directed graph is a vertex that only features outgoing edges; a sink vertex only incident edges. This definition can be directly mapped to the hydrologic context with out-/in-flowing surface water. Locations of source vertices are assumed to be drier, whereas locations of sink vertices would be considered more likely to inundate (disregarding vertical drainage through the soil).
- *Number of connected components.* In the graph, each connected component corresponds to a hydrologically isolated network. Small isolated components with only few edges are likely to have only recently formed. Water in these areas is not able to drain from the landscape until further troughs have initiated and connected with nearby components.
- *Betweenness centrality.* For every pair of vertices within a connected component of the directed graph we calculate the shortest path. We use Dijkstra's method [11] and take into account the edge weights describing the real-world length of each channel. If we assume that water follows the shortest path[1], we can further determine the betweenness centrality for each edge. With Brande's implementation [6], this metric is defined by $C_b = \sum_{s,t \in V} \frac{\sigma(s,t|v)}{\sigma(s,t)}$, with $\sigma(s,t)$ corresponding to the number of shortest paths and $\sigma(s,t|v)$ the number of shortest paths traversing vertex v, with $v \neq s$ and $v \neq t$. We expect higher betweenness centralities for vertices surrounding edges that singly connect two (almost) isolated networks. These edges pinpoint troughs that are most likely to be responsible for network drainage and further experience higher discharge rates [25]. The latter might also indicate higher potential for further erosion of trough walls.
- *Network density.* The density d gives an estimate of the network flow effectiveness. It is defined as $d = \frac{e_e}{e_p}$, with e_e being the number of edges within the graph and e_p the number of all possible edges. In planar graphs $e_p = 3(n-1)$ is valid. For permafrost landscapes however, Cresto-Aleina et al. [8] have shown that it is possible to approximate the polygonal patterns with Voronoi diagrams, and we thus assume $e_p = \frac{3}{2}(n+1)$.

While all computational steps in the first two modules of the introduced approach (Chapter 3.1 and 3.2) generally scale linearly, the third module with graph analysis algorithms (Chapters 3.3) do slightly worse. Determining the centrality scales with $O(e \cdot \log n)$ and computing shortest path lengths even requires $O(n^3)$.

4 EXPERIMENTS

We conducted experiments with very-high-resolution (1 m/px) digital terrain models derived from laserscanning elevation data. Our analysis focuses on characterizing the temporal evolution of a degrading landscape, and we thus require terrain data from a minimum of two different dates of the same site. Unfortunately, terrain models at this high spatial resolution are rather scarce, as acquisition requires costly campaigns with scientific grade sensors aboard specialized airplanes or UAV. In remote regions such as the Arctic, especially repeat surveys are therefore rare. The study area for the experiments conducted here is thus constrained to approximately 1 km^2 in a fire scar (fire burned in 2007) in Northslope, Alaska, USA. For this site, appropriate laserscanning terrain models at 1 m resolution are available from the summers of 2009, 2014 and 2019. Fig. 1 shows the digital terrain model of 2019.

We set up our experiments on a modern Windows 10 workstation with Intel(R) Xeon(R) E5-2650 v4 CPU at 2.20 GHz and 64 GB of RAM. All code was implemented with Python 3.8.

4.1 From Images to Graphs

Previously, we mentioned that image pre-processing, skeletonization, and graph extraction all roughly scale with $O(n \cdot m)$ with n and m being the height and width of the input image in pixels. However, we must acknowledge that the execution time of the morphological image algorithms on the binarized data also depends on the complexity of the foreground pattern (i.e., the trough network) and the thickness of the strokes [43]. While implemented in parallel, the thinning operations are nevertheless an iterative process. For our input datasets of size 877 px by 730 px, we thus observe runtimes between 5 and 7.5 s per image for generating the skeleton and extracting the graph as described in the first module. The input image of 2009, with fewer troughs to segment, settles at the lower end of this scale, while the images from 2014 and 2019 with the rougher landscapes and higher numbers of troughs require slightly more time.

To validate the accuracy of our analytical trough segmentation approach, we manually traced the location of troughs from a 300 m by 300 m (at 1 m^2 this corresponds to an input dataset of 300 px by 300 px) subset of the 2019 input array (Fig. 4 a). We computed the skeleton of this manual delineation (Fig. 4 b) and overlaid the automatically segmented skeleton (Fig. 4 c and d). We are only interested in the number of true positives over the number of total positives and thus declare the accuracy based on the sensitivity. In this case, the sensitivity yields a result of only 0.17. However, since we are later looking at transects of length X px (in this study $X = 13$, which lie perpendicular to the trough skeleton, described in Chapter 4.2), we are able to capture information on channel morphologies that are located in the $X/2$ px-vicinity to each side of the skeleton (Fig. 4 e). Thus, computing the accuracy for segmentation considering this larger field of view, we achieve a sensitivity of 0.84.

As with most automated image classification or segmentation tasks, building a ground truth or training data base is a biased task. Even experts in the field, manually labeling or delineating real-world images, will introduce biases that could differ from another expert's interpretation of the same image. Especially considering the images in this study, with the dynamic landscapes in transition, it is difficult to determine at which point a polygon border has subsided far enough to be considered a trough. Based on the sensitivity of 0.84 when considering the larger field of view (Fig. 4e), we can interpret that the analytical segmentation algorithm was slightly more conservative than the expert's segmentation and did not pick up on some troughs that are only just initiating. It can

[1]We acknowledge that this might not be hydrologically correct. For very flat terrains (as is often the case in similar permafrost landscapes), we can however assume this flow behavior as first-order approximation.

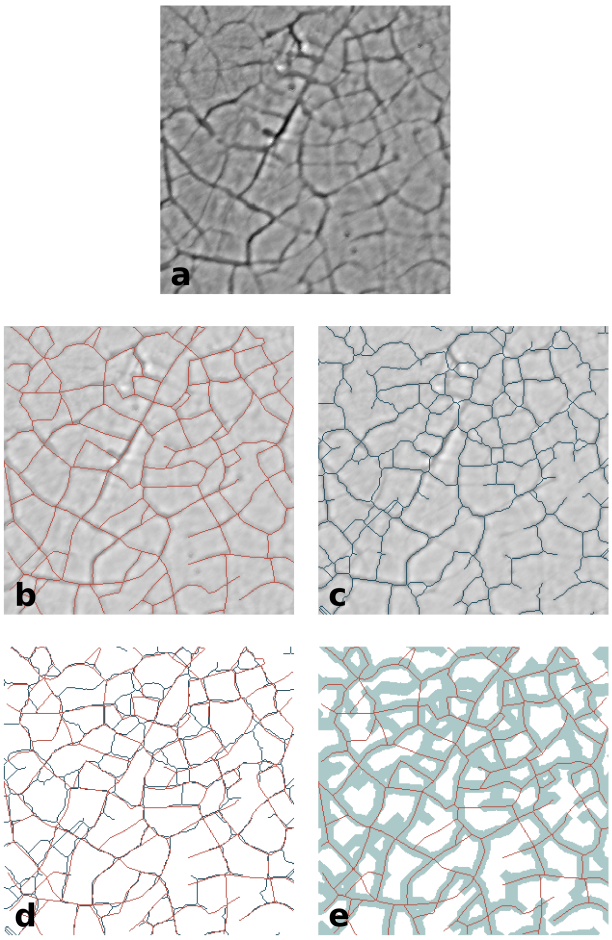

Figure 4: Validation workflow. (a) Digital terrain model of the 300 m by 300 m validation area subset. Darker colored pixels represent relative lower elevations, brighter colors represent relative higher elevations. (b) Red lines show the manually delineated 'ground truth' as determined by the authors. The terrain model from (a) is shown in the background for reference. (c) Blue lines represent the skeleton of the trough network as computed by the analytical approach described in Chapter 3.1. The terrain model from (a) is shown in the background for reference. (d) Manually determined ground truth in red from (b) overlain with automatically extracted skeleton in blue from (c) to visualize the success of the introduced extraction approach. (e) Manual trough delineation (in red), overlain by the $X/2$ px-vicinity of the automatically segmented troughs (faint blue). As we also investigate the surroundings of the trough skeleton to analyze trough morphologies (see Chapter 3.2), we consider the automated trough segmentation to be successful whenever the ground truth troughs lie within this $X/2$ px-vicinity.

Table 1: Comparison of graph metrics describing the trough network evolution in the investigated permafrost landscape between 2009 and 2019. Results underline the consistent network growth as well the increasing connectivity over time.

	2009	2014	2019
# edges	1292	2428	2585
average node degree	2.15	2.44	2.63
% sources	36.14	26.86	22.96
% sinks	21.73	19.43	13.24
# connected components	72	14	6
betweenness centrality	0.91e-5	1.64e-5	4.96e-5
network density	0.72	0.81	0.88
total channel length [km]	13.45	36.68	40.74

certainly be argued among experts as well, if these onsets should already be considered troughs. Based on the large range of possible interpretations of ground truth, we thus accept a sensitivity of 0.84 as sufficient for the ongoing analysis.

4.2 From Terrain Properties to Graph Parameters

As fitting a Gaussian function through a non-linear least squares approximation to e_p transects is rather compute intensive, we parallelized this task (see Chapter 3.2). We constrained the least-squares optimizer to $5 \cdot 10^5$ iterations for finding the best fitting parameter. With distributing the optimization to 20 cores we could thus achieve runtimes of approximately $3.85 \cdot 10^{-5} \cdot e_p$ seconds.

Fig. 5 shows some exemplary transects with their fitted Gaussian and the parameters of FWHM and $f(\mu)$ corresponding to the trough widths and heights respectively. We further compared the median morphologies for the three analyzed years and found that the width has increased from 5.6 m to 7.7 m between 2009 and 2019. Within the locations where we found troughs in 2009, the median trough depth has also increased by 0.05 m. However, considering the slight vertical inaccuracies of the terrain model, this result is not considered significant.

Manually measuring the troughs' depths and widths either in the field or extracting this information from imagery to generate ground truth values is not clearly defined, as troughs rarely show clear-cut vertical walls, but usually gently slope into the landscape. Thus, determining the start and endpoints where to measure the 'true' depths and widths can vary from user to user, and we cannot provide a detailed assessment on the accuracy of the results derived above. However, our findings are all in line with the observations made by multiple different experts in such thaw-affected landscapes [19, 34, 40]. This shows that by approximating the trough morphology with a Gaussian curve, we introduce a robust, transferable, and especially scalable methodology to better describe trough characteristics in future studies.

4.3 From Graphs to Hydrology

Analyzing the graphs from the three investigated years (2009, 2014, and 2019), we found very consistent trends. Table 1 gives an overview of the graph metrics of interest as described in Chapter 3.3.

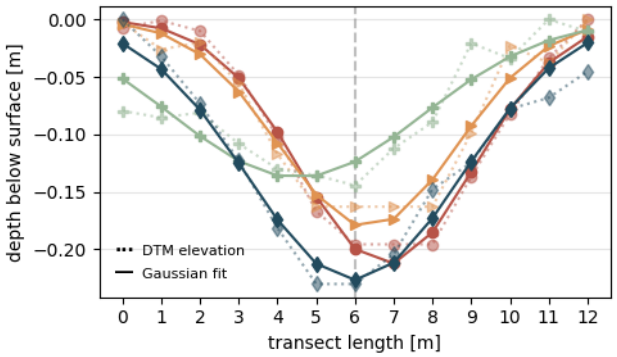

Figure 5: Exemplary cross-sections extracted along four different troughs showing the measured absolute elevation profiles (as taken from the digital terrain model) and the optimized Gaussian function fitted to the data points of the same color (solid line). The vertical, grey guideline at 6 m represents the center of the transect and thus visualizes the location of the skeleton pixel that determined the transect positioning. We observe the Gaussian is able to approximate transects also for locations where the trough skeleton pixel did not capture the lowest point of the channel (e.g., green/cross and red/circle transects).

For one, we observe a significant increase in the overall size of the graphs. Between 2009 and 2019, the number of edges has doubled in the study region. While directly linked to this increase, the total length of potential pathways for hydrological surface flow has tripled in this time period (total channel length). This underlines that especially longer troughs tend to initiate only later on, or that troughs not only grow in depth and width, but also in length. Further, we also identify a strong increase in the connectivity of the trough network. The increasing average node degree and the decreasing percentage of source and sink vertices (dead-end troughs), shows that troughs which have initiated in the early years (but maybe only connected to one polygon intersection), have then degraded further so that water is able to flow between two intersections (two nodes). Seeing the remarkable decrease of total number of connected components in the study area drop from more than 70 to only six components, strongly underlines the increasing landscape connectivity, and thus in this scenario, also its degradation. The metric of network density also gives valuable insights towards this characteristic. Based on the assumption that the underlying ice-wedge networks can be approximated with Voronoi diagrams (and thus correspond to a network density of 1; see Chapter 3.3, [8]), we assume that the fully degraded network, that is, when all troughs have initiated, also renders a network density of 1. With 72% of troughs initiated in 2009, to almost 90% of troughs present ten years later, we observe a notable step towards maximum connectivity of the hydrologic network.

Overall, we observe that the majority of the changes witnessed occurred between 2009 and 2014 but seemed to decelerate in the years after. This leads to believe that landscape responses to tundra fires are immediate and pronounced, but can stabilize after several years, underlining observations made with other methodologies [18–20]. For further analysis on the environmental changes observed with this approach, please refer to Rettelbach et al. [31].

5 CONCLUSION AND FUTURE WORK

In this study, we presented a highly modular and automated approach to analyze digital terrain models, which are represented as two-dimensional images with grayscale values, for determining the state of degradation in thaw-affected permafrost landscapes. With computer vision, we extract elevation information from data stored as arrays and represent the characteristic polygonal network landscape as graphs. Simply by reshaping the way we represent the information, we obtain access to an entirely new suite of analysis methods and thus gain a new perspective with unprecedented quantitative detail of the geomorphological and hydrological characteristics of these Arctic landscapes. Graphs are further more efficient in storage properties than images, but we must of course acknowledge that non-network-related information is lost in the conversion process. However, the newly derived morphological properties and network quantities can further be seen as valuable measures for integration into numerical models of permafrost degradation processes. Both represent important progress for furthering our understanding of the complex interactions between thawing permafrost landscapes and our changing climate.

Generally, we aim to enable this type of analysis for the pan-Arctic scale, however, our approach requires the input data to satisfy two main characteristics: (i) The elevation model needs to hold information on the elevation of the bare ground and not on that of the surface (i.e., top-of-vegetation, infrastructure, buildings). And (ii), the data needs to be at a very high spatial resolution ($\leq$1 m/px), since we investigate structures with high spatial detail. As it is currently almost only possible to gather this type of data by aerial surveys with sensors mounted aboard UAV or aircraft, acquisition is very costly - both temporally and financially, and it is spatially limited. To the best of our knowledge, there currently exists no comprehensive database of appropriate elevation datasets for the entire Arctic. The best pan-Arctic dataset currently available is the ArcticDEM [29] with 2 m pixel resolution. However, it does not represent bare ground elevation information, but includes canopy and snow, as it is derived from stereophotogrammetric processing of very-high-resolution satellite imagery; thus not satisfying requirement (i). Nevertheless, a multitude of local and regional elevation datasets with appropriate very-high resolution are increasingly becoming available through various research and mapping projects in permafrost regions.

In the future, we might gain access to this kind of data across larger regions either through optimizing the optical properties of sensor technologies and enabling higher resolutions from satellite-based missions, or by enhancing already available data through e.g., super-resolution algorithms. Until then, our methodology can at least enable valuable insights into areas for which we do have access to appropriate data already.

Through the highly modular setup, we further promote the interchangeability of single substeps. This allows easy adaptation of our approach to the user's individual data pre-requisites or analysis

needs. For example, a user might prefer a deep-learning-based polygon segmentation method in module 1, or work in a considerably different area where troughs might be even better approximated with other non-linear functions (substitution of optimization function in module 2), or be interested in slightly different network parameters (addition of graph metrics in module 3).

Overall, we here introduced a largely automated and scalable approach that considerably facilitates access to new and valuable insights for permafrost research, and thus enables quantification of its impact on hydrology, ecology, and the climate.

ACKNOWLEDGMENTS

We would like to begin by acknowledging and thanking the Iñupiat, on whose traditional territory we were able to collect data and conduct research for this manuscript. Financially, this work was supported by Geo.X, the Research Network for Geosciences in Berlin and Potsdam. T.R. acknowledges the support by the Helmholtz Einstein International Berlin Research School in Data Science (HEIBRiDS). B.M.J. was supported by a grant from the US National Science Foundation (NSF OIA-1929170). We acknowledge support by the Open Access Publication Funds of the Alfred Wegener Institute Helmholtz Centre for Polar and Marine Research. We further thank Martin Gehrmann, Maximilian Stöhr, Matthias Gessner, Torsten Sachs, and the Kenn Borek Air pilot crew, who supported data acquisition during the airborne flight campaign with AWI's Polar-5 research airplane. Many thanks also go to Brian Groenke for his helpful comments and to Blake Robert Mills for introducing the MetBrewer color palette.

REFERENCES

[1] Charles J Abolt, Michael H Young, Adam L Atchley, and Cathy J Wilson. 2019. Brief communication: Rapid machine-learning-based extraction and measurement of ice wedge polygons in high-resolution digital elevation models. *The Cryosphere (Online)* 13, LA-UR-18-29238 (2019).

[2] Werner Baumgarten and Marcus J Hauser. 2010. Detection, extraction, and analysis of the vein network. *Journal of Computational Interdisciplinary Sciences* 1, 3 (2010), 241–249.

[3] Md Abul Ehsan Bhuiyan, Chandi Witharana, and Anna K Liljedahl. 2020. Use of Very High Spatial Resolution Commercial Satellite Imagery and Deep Learning to Automatically Map Ice-Wedge Polygons across Tundra Vegetation Types. *Journal of Imaging* 6, 12 (2020), 137.

[4] Robert F Black. 1976. Periglacial features indicative of permafrost: ice and soil wedges. *Quaternary Research* 6, 1 (1976), 3–26.

[5] G. Bradski. 2000. The OpenCV Library. *Dr. Dobb's Journal of Software Tools* (2000).

[6] Ulrik Brandes. 2001. A faster algorithm for betweenness centrality. *Journal of mathematical sociology* 25, 2 (2001), 163–177.

[7] RJE Brown and WO Kupsch. 1975. Permafrost Terminology. *Quaternary Research* 5, 3 (1975), 468.

[8] Fabio Cresto-Aleina, Victor Brovkin, S Muster, J Boike, Lars Kutzbach, Torsten Sachs, and Sergei Zuyev. 2013. A stochastic model for the polygonal tundra based on Poisson-Voronoi diagrams. *Earth System Dynamics* 4, 2 (2013), 187–198.

[9] Jonathan A Czuba and Efi Foufoula-Georgiou. 2015. Dynamic connectivity in a fluvial network for identifying hotspots of geomorphic change. *Water Resources Research* 51, 3 (2015), 1401–1421.

[10] Stijn Dhondt, Dirk Van Haerenborgh, Caroline Van Cauwenbergh, Roeland MH Merks, Wilfried Philips, Gerrit TS Beemster, and Dirk Inzé. 2012. Quantitative analysis of venation patterns of Arabidopsis leaves by supervised image analysis. *The Plant Journal* 69, 3 (2012), 553–563.

[11] Edsger W Dijkstra et al. 1959. A note on two problems in connexion with graphs. *Numerische mathematik* 1, 1 (1959), 269–271.

[12] Jiajie Feng, Cong Wang, Jiesi Lei, Yunfeng Yang, Qingyun Yan, Xishu Zhou, Xuanyu Tao, Daliang Ning, Mengting M Yuan, Yujia Qin, et al. 2020. Warming-induced permafrost thaw exacerbates tundra soil carbon decomposition mediated by microbial community. *Microbiome* 8, 1 (2020), 1–12.

[13] Aric Hagberg, Pieter Swart, and Daniel S Chult. 2008. *Exploring network structure, dynamics, and function using NetworkX.* Technical Report. Los Alamos National Lab.(LANL), Los Alamos, NM (United States).

[14] Charles R. Harris, K. Jarrod Millman, Stéfan J van der Walt, Ralf Gommers, Pauli Virtanen, David Cournapeau, Eric Wieser, Julian Taylor, Sebastian Berg, Nathaniel J. Smith, Robert Kern, Matti Picus, Stephan Hoyer, Marten H. van Kerkwijk, Matthew Brett, Allan Haldane, Jaime Fernández del Río, Mark Wiebe, Pearu Peterson, Pierre Gérard-Marchant, Kevin Sheppard, Tyler Reddy, Warren Weckesser, Hameer Abbasi, Christoph Gohlke, and Travis E. Oliphant. 2020. Array programming with NumPy. *Nature* 585 (2020), 357–362. https://doi.org/10.1038/s41586-020-2649-2

[15] David G Harry and Jan S Gozdzik. 1988. Ice wedges: growth, thaw transformation, and palaeoenvironmental significance. *Journal of Quaternary Science* 3, 1 (1988), 39–55.

[16] Songtao He, Favyen Bastani, Satvat Jagwani, Mohammad Alizadeh, Hari Balakrishnan, Sanjay Chawla, Mohamed M Elshrif, Samuel Madden, and Mohammad Amin Sadeghi. 2020. Sat2graph: Road graph extraction through graph-tensor encoding. In *European Conference on Computer Vision*. Springer, 51–67.

[17] Gustaf Hugelius, Jens Strauss, Sebastian Zubrzycki, Jennifer W Harden, Edward AG Schuur, Chien-Lu Ping, Lutz Schirrmeister, Guido Grosse, Gary J Michaelson, Charles D Koven, et al. 2014. Estimated stocks of circumpolar permafrost carbon with quantified uncertainty ranges and identified data gaps. *Biogeosciences* 11, 23 (2014), 6573–6593.

[18] Go Iwahana, Masao Uchida, Lin Liu, Wenyu Gong, Franz J Meyer, Richard Guritz, Tsutomu Yamanokuchi, and Larry Hinzman. 2016. InSAR detection and field evidence for thermokarst after a tundra wildfire, using ALOS-PALSAR. *Remote Sensing* 8, 3 (2016), 218.

[19] Benjamin M Jones, Amy L Breen, Benjamin V Gaglioti, Daniel H Mann, Adrian V Rocha, Guido Grosse, Christopher D Arp, Michael L Kunz, and Donald A Walker. 2013. Identification of unrecognized tundra fire events on the north slope of Alaska. *Journal of Geophysical Research: Biogeosciences* 118, 3 (2013), 1334–1344.

[20] Benjamin M Jones, Guido Grosse, Christopher D Arp, Eric Miller, Lin Liu, Daniel J Hayes, and Christopher F Larsen. 2015. Recent Arctic tundra fire initiates widespread thermokarst development. *Scientific reports* 5 (2015), 15865. https://www.ncbi.nlm.nih.gov/pmc/articles/PMC4625366/pdf/srep15865.pdf

[21] Ernest de K Leffingwell. 1915. Ground-ice wedges: The dominant form of ground-ice on the north coast of Alaska. *The Journal of Geology* 23, 7 (1915), 635–654.

[22] Kwan-tai Leung and Zoltán Néda. 2010. Criticality and pattern formation in fracture by residual stresses. *Physical Review E* 82, 4 (2010), 046118.

[23] Anna K Liljedahl, Julia Boike, Ronald P Daanen, Alexander N Fedorov, Gerald V Frost, Guido Grosse, Larry D Hinzman, Yoshihiro Iijma, Janet C Jorgenson, and Nadya Matveyeva. 2016. Pan-Arctic ice-wedge degradation in warming permafrost and its influence on tundra hydrology. *Nature Geoscience* 9, 4 (2016), 312–318.

[24] J Ross Mackay. 1990. Some observations on the growth and deformation of epigenetic, syngenetic and anti-syngenetic ice wedges. *Permafrost and Periglacial Processes* 1, 1 (1990), 15–29.

[25] Wouter A Marra, Maarten G Kleinhans, and Elisabeth A Addink. 2014. Network concepts to describe channel importance and change in multichannel systems: test results for the Jamuna River, Bangladesh. *Earth Surface Processes and Landforms* 39, 6 (2014), 766–778.

[26] Carmody K McCalley, Ben J Woodcroft, Suzanne B Hodgkins, Richard A Wehr, Eun-Hae Kim, Rhiannon Mondav, Patrick M Crill, Jeffrey P Chanton, Virginia I Rich, Gene W Tyson, et al. 2014. Methane dynamics regulated by microbial community response to permafrost thaw. *Nature* 514, 7523 (2014), 478–481.

[27] Jaroslav Obu. 2021. How much of the Earth's surface is underlain by permafrost? *Journal of Geophysical Research: Earth Surface* (2021), e2021JF006123.

[28] Jaroslav Obu, Sebastian Westermann, Annett Bartsch, Nikolai Berdnikov, Hanne H Christiansen, Avirmed Dashtseren, Reynald Delaloye, Bo Elberling, Bernd Etzelmüller, and Alexander Kholodov. 2019. Northern Hemisphere permafrost map based on TTOP modelling for 2000–2016 at 1 km2 scale. *Earth-Science Reviews* 193 (2019), 299–316.

[29] Claire Porter, Paul Morin, Ian Howat, Myoung-Jon Noh, Brian Bates, Kenneth Peterman, Scott Keesey, Matthew Schlenk, Judith Gardiner, Karen Tomko, Michael Willis, Cole Kelleher, Michael Cloutier, Eric Husby, Steven Foga, Hitomi Nakamura, Melisa Platson, Jr. Wethington, Michael, Cathleen Williamson, Gregory Bauer, Jeremy Enos, Galen Arnold, William Kramer, Peter Becker, Abhijit Doshi, Cristelle D'Souza, Pat Cummens, Fabien Laurier, and Mikkel Bojesen. 2018. ArcticDEM. https://doi.org/10.7910/DVN/OHHUKH

[30] Charles A Price, Olga Symonova, Yuriy Mileyko, Troy Hilley, and Joshua S Weitz. 2011. Leaf extraction and analysis framework graphical user interface: segmenting and analyzing the structure of leaf veins and areoles. *Plant Physiology* 155, 1 (2011), 236–245.

[31] Tabea Rettelbach, Moritz Langer, Ingmar Nitze, Benjamin Jones, Veit Helm, Johann-Christoph Freytag, and Guido Grosse. 2021. A Quantitative Graph-Based Approach to Monitoring Ice-Wedge Trough Dynamics in Polygonal Permafrost Landscapes. *Remote Sensing* 13, 16 (2021), 3098.

[32] Edward AG Schuur, A David McGuire, C Schädel, Guido Grosse, Jennifer W Harden, Daniel J Hayes, Gustaf Hugelius, Charles D Koven, Peter Kuhry, David M Lawrence, et al. 2015. Climate change and the permafrost carbon feedback. *Nature* 520, 7546 (2015), 171–179.

[33] Pierre Soille. 2013. *Morphological image analysis: principles and applications*. Springer Science & Business Media.

[34] Mathias Ulrich, Ernst Hauber, Ulrike Herzschuh, Stefanie Härtel, and Lutz Schirrmeister. 2011. Polygon pattern geomorphometry on Svalbard (Norway) and western Utopia Planitia (Mars) using high-resolution stereo remote-sensing data. *Geomorphology* 134, 3-4 (2011), 197–216.

[35] Stefan Van der Walt, Johannes L Schönberger, Juan Nunez-Iglesias, François Boulogne, Joshua D Warner, Neil Yager, Emmanuelle Gouillart, and Tony Yu. 2014. scikit-image: image processing in Python. *PeerJ* 2 (2014), e453.

[36] Gael Varoquaux and Loic Esteve. 2020. *Joblib: running Python functions as pipeline jobs*. https://joblib.readthedocs.io/

[37] Pauli Virtanen, Ralf Gommers, Travis E. Oliphant, Matt Haberland, Tyler Reddy, David Cournapeau, Evgeni Burovski, Pearu Peterson, Warren Weckesser, Jonathan Bright, Stéfan J. van der Walt, Matthew Brett, Joshua Wilson, K. Jarrod Millman, Nikolay Mayorov, Andrew R. J. Nelson, Eric Jones, Robert Kern, Eric Larson, C J Carey, İlhan Polat, Yu Feng, Eric W. Moore, Jake VanderPlas, Denis Laxalde, Josef Perktold, Robert Cimrman, Ian Henriksen, E. A. Quintero, Charles R. Harris, Anne M. Archibald, Antônio H. Ribeiro, Fabian Pedregosa, Paul van Mulbregt, and SciPy 1.0 Contributors. 2020. SciPy 1.0: Fundamental Algorithms for Scientific Computing in Python. *Nature Methods* 17 (2020), 261–272. https://doi.org/10.1038/s41592-019-0686-2

[38] Matthias P Wagner and Natascha Oppelt. 2020. Extracting agricultural fields from remote sensing imagery using graph-based growing contours. *Remote Sensing* 12, 7 (2020), 1205.

[39] Zifeng Wang, Jinbao Li, Yi Lin, Ying Meng, and Junguo Liu. 2020. GrabRiver: Graph-Theory-Based River Width Extraction From Remote Sensing Imagery. *IEEE Geoscience and Remote Sensing Letters* (2020).

[40] Melissa K Ward Jones, Wayne H Pollard, and Frances Amyot. 2020. Impacts of Degrading Ice-Wedges on Ground Temperatures in a High Arctic Polar Desert System. *Journal of Geophysical Research: Earth Surface* 125, 3 (2020), e2019JF005173.

[41] Chandi Witharana, Md Abul Ehsan Bhuiyan, Anna K Liljedahl, Mikhail Kanevskiy, Torre Jorgenson, Benjamin M Jones, Ronald Daanen, Howard E Epstein, Claire G Griffin, Kelcy Kent, et al. 2021. An Object-Based Approach for Mapping Tundra Ice-Wedge Polygon Troughs from Very High Spatial Resolution Optical Satellite Imagery. *Remote Sensing* 13, 4 (2021), 558.

[42] Yan Xiaolong and Charles N. Christensen. 2021. *Skeleton Network*. https://github.com/Image-Py/sknw

[43] Tongjie Y Zhang and Ching Y. Suen. 1984. A fast parallel algorithm for thinning digital patterns. *Commun. ACM* 27, 3 (1984), 236–239.

[44] Weixing Zhang, Chandi Witharana, Anna K Liljedahl, and Mikhail Kanevskiy. 2018. Deep convolutional neural networks for automated characterization of arctic ice-wedge polygons in very high spatial resolution aerial imagery. *Remote Sensing* 10, 9 (2018), 1487.